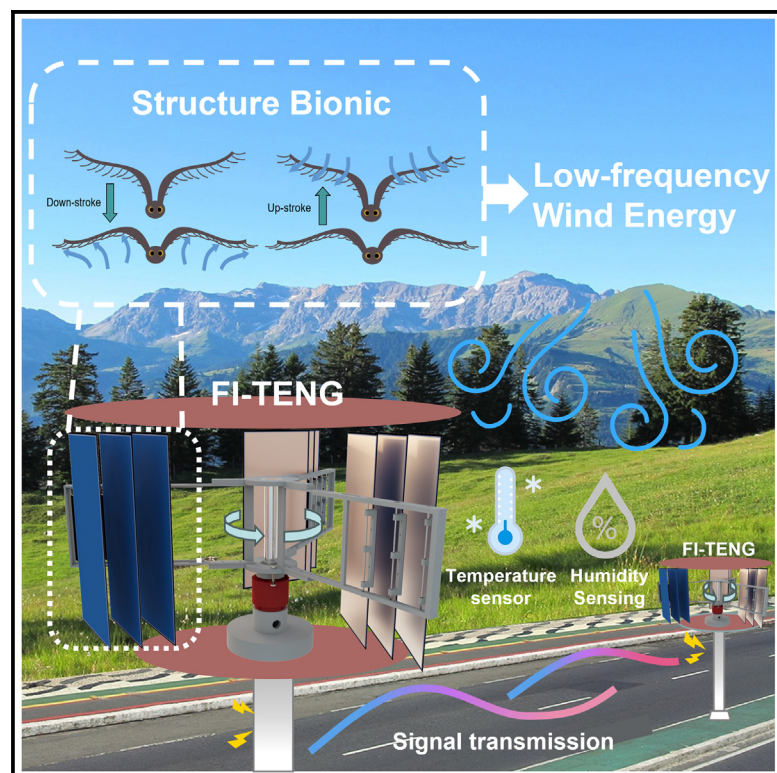# Article

Feather-inspired triboelectric nanogenerator with lift and drag modulation for wind energy harvesting

Graphical abstract

Authors

Zhenxing Ding, Erming Su, Hongbo Yang, Zhanyong Hong, Zhong Lin Wang, Leo N.Y. Cao

Correspondence

zhong.wang@mse.gatech.edu (Z.L.W.), caonanying@binn.cas.cn (L.N.Y.C.)

In brief

We developed a multilayer flapping triboelectric nanogenerator (TENG), inspired by the interlocking mechanism of bird flight feathers, designed to efficiently capture breeze energy. Its lift-and-drag modulation feature ensures low wear and a start-up wind speed of only 0.5 m/s. We anticipate that TENGs will enable remote environmental monitoring and facilitate the interconnection of environmental data across different regions.

Highlights

- A multilayer flapping biomimetic triboelectric nanogenerator (TENG) is developed

- The TENG's structure and mechanism mimic the dynamics of birds' flight feathers

- The lift-and-drag modulation allows low wear and a start-up wind speed at 0.5 m/s

- Pressure and velocity distributions are numerically simulated and investigated

Validate
Functional device with real-world testing, ready to scale

CellPress

Device

CellPress
OPEN ACCESS

Article

Feather-inspired triboelectric nanogenerator with lift and drag modulation for wind energy harvesting

Zhenxing Ding,[1,2,3] Erming Su,[2,4] Hongbo Yang,[2] Zhanyong Hong,[1,2] Zhong Lin Wang,[1,2,4,*] and Leo N.Y. Cao[1,2,4,5,*]

[1]Guangzhou Institute of Blue Energy, Knowledge City, Huangpu District, Guangzhou 510555, P.R. China
[2]CAS Center for Excellence in Nanoscience, Beijing Key Laboratory of Micro-nano Energy and Sensor, Beijing Institute of Nanoenergy and Nanosystems, Chinese Academy of Sciences, Beijing 101400, P.R. China
[3]College of Geography and Environmental Sciences, Zhejiang Normal University, Jinhua 321000, P.R. China
[4]School of Nanoscience and Technology, University of Chinese Academy of Sciences, Beijing 100049, P.R. China
[5]Lead contact
*Correspondence: zhong.wang@mse.gatech.edu (Z.L.W.), caonanying@binn.cas.cn (L.N.Y.C.)
https://doi.org/10.1016/j.device.2024.100571

THE BIGGER PICTURE Triboelectric nanogenerators (TENGs) are devices that convert mechanical energy, for example, from the wind, ocean waves, and human motion, into electricity. However, harvesting energy from low winds or unstable and irregular sources of energy as the motion is challenging mainly due to the devices' low energy conversion efficiency and the high friction, which causes high starting wind speed. To capture energy from even gentle breezes, we developed a bird feather-inspired TENG that functions as a wind harvester and alternator simultaneously, converting wind energy into power at very low wind speeds. This technology can be used in outdoor areas for environmental monitoring and for the support of potential networks that record various parameters in places like valleys and hills.

SUMMARY

Inspired by the interlocking mechanism of bird flight feathers in nature, we have developed feather-inspired triboelectric nanogenerators (FI-TENGs) in the form of vertical wind blades with lift and drag modulation for wind energy harvesting. The unidirectional locking structure of this blade can compensate for the limitations of the wind turbine in collecting low-speed wind energy. A single FI-TENG can start at 0.5 m s^{-1} breeze and can reach a peak power of 2.36 mW at 2.5 m s^{-1}. With proper design and optimization, the FI-TENG can generate energy to power alarm indicators and environmental sensors.

INTRODUCTION

Triboelectric nanogenerator (TENG) converts mechanical energy in the environment, including wind energy,[1–5] ocean wave energy,[6,7] and human movement,[8] into electrical energy by coupling contact electrification and electrostatic induction.[9,10] Low-frequency, random, and irregular energy from the surrounding environment (e.g., human motion, wind, ocean waves) can be used to power the device or as a fully self-driven energy supply for the sensor.[11] TENG has the advantages of simple manufacturing,[12] light weight,[13] low cost,[14] wide choice of materials,[15–17] high durability,[18–20] and environment adaptability.[21,22] Although TENGs have made advances in the field of low-frequency wind energy collection, due to structural constraints, most of the reports focus on high wind speeds, with start-up wind speeds above 2 m s^{-1}, which leaves a gap for breeze energy harvesting.[23–27]

Here, we present a feather-inspired multilayer flapping TENG (FI-TENG) with a high lift-to-drag ratio (L/D). In aerodynamics, the L/D is a key performance metric that compares the amount of lift force generated by an aerodynamic surface to the force acting opposite to the motion, known as the drag force. Each blade of the FI-TENG experiences high lift when facing the headwind and reduced drag when positioned on the opposite (downwind side), leading to high energy conversion efficiency and an L/D of 45 (compared to less than 11 for normal airfoils).[28,29] The power-generation unit with low-triboelectric slip ring is integrated with the feather structure for optimal performance. The FI-TENG operates in the contact-separation mode, promoting low wear and starting wind speed under various wind speed conditions. The five-layer composite blades of the FI-TENG maintain consistent blade movement, providing stable energy output. We analyzed the pressure and flow velocity distributions of the blades, mimicking the one-way air passage mechanism of

Device
Article

feathers. Wind tests demonstrated a start-up wind speed as low as 0.5 m s^{-1} and a maximum output at 2.5 m s^{-1}, with peak power reaching 2.36 mW. FI-TENG can be used in valleys and hills and may provide power for the Internet of Things sensor network for constant environmental monitoring.

RESULTS AND DISCUSSION

Structural design and working principle of the FI-TENG

FI-TENG combines biomimicry and TENG principles with its design and working principle explained through three sections. To begin, we elucidate the bionic principles involved in the closing and unfolding of feathers during bird locomotion. Subsequently, we employ the design concept of feather closure structure to construct a similar structure with identical functionality (Figure 1). Next, we determine the charge and current distribution between the blades from the TENG perspective. Finally, we use COMSOL Multiphysics simulation to analyze the pressure and velocity distributions of the FI-TENG and obtain an equivalent L/D (Figure 2).

FI-TENG mimicking bird flight feather mechanics

Flight feathers facilitate the airborne capabilities of birds by providing high lift during wing flapping through coordinated flapping and passive orientation adjustment,[30] the key mechanism that inspired our FI-TENG design for efficient wind energy harvesting. The flight feather comprises three main parts: the feather shaft, the feather branch, and the feather root, as illustrated in Figure 1A. The movement pattern of feathers in birds is illustrated in Figures 1B–1I. The downward movements of a bird's wings (downstroke) generate an upward high lift force under the wings that enables the bird to maintain stability or ascend, while the upward flap (upstroke) offers a low drag resistance and resets the wing for the next downward flap, thanks to the one-way air passage feature. More specifically, during the upstroke, each feather rotates around the shaft and opens the feather array, allowing the air to pass through the feather branches and reducing drag (see inset of Figures 1B–1Bii). During the downstroke, the upward force from the air leads to the interlocking of the feather branches to provide lift.[31]

Inspired by the one-way air passage mechanism of the feathers, we designed an FI-TENG structure as shown in Figure 1C according to the movement patterns of birds' feathers. In general, the FI-TENG has three groups of vertical flaps that rotate around a vertical shaft. Each group is mounted on an arm spaced 120° apart, with each group containing three flaps that are free to rotate around their vertical pins. In detail, the TENG comprises four main parts: a three-dimensional (3D)-printed polylactic acid (PLA) outer frame for securing the feather structure, a load-bearing central axis to maintain device orientation, a triboelectric power-generating unit, and a conductive slip ring for energy collection and conversion. The main components are the nine composite triboelectric layer blades (three blades per group), serving as both the wind harvester and the energy generator. Figure 1D illustrates the composite layer of the blade consisting of polytetrafluoroethylene (PTFE), Cu, carbon fiber, and polyurethane sponge. To increase the contact area between

the blades, polyurethane sponge is laminated on both sides of the carbon fiber backing as the cushioning material. Furthermore, the outer surface of the polyurethane sponge is laminated with Cu-PTFE and Cu, respectively. To ensure equal quality and size, we used a carbon fiber plate measuring 10 × 20 cm as the underlay, which is shown in Figure 1E. The slip ring collects energy at the blade end and transfers it to a fixed power management circuit at the other end. Compared with traditional wind harvesting TENGs, where the wind harvester and power generator parts are separated, the FI-TENG works as both the wind harvester and the power generator, reducing system weight, size, and friction. The structural advantage results in lower start-up wind speeds in the mild fluid regime as low as 0.5 m s^{-1}, as shown in Figure 1F.[23–26,32–35] Additional information regarding the fabrication process is available in the experimental procedures.

Working principle of the FI-TENG

The coupling of triboelectric effect and electrostatic induction is the operating principle for TENG. In the case of FI-TENG, its operating mechanism specifically utilizes the contact-separation mode, where two electrodes attached with opposite polarity materials come into contact and separate according to mechanical stimulation.[9] Figure 2A explains the distribution of charge and current that occurs during the contact and separation. The Cu film attached to the right side of blade 1 acts as an electrode and a triboelectric layer, referred to as electrode A. Similarly, the left side of the blade has a Cu film, referred to as electrode B. The surface of electrode B is covered with a PTFE film, which acts as an additional layer of triboelectric material. Initially, electrode A contacts the PTFE membrane, creating an induced charge on the contact surface that maintains the charge balance (Figure 2A, state i). As the back of the blade rotates to the windward side and separation begins, the PTFE membrane surface generates a certain amount of negative charge due to its greater ability to attract negative charges. When free electrons are transferred from electrode B to electrode A through an external load (e.g., a connected device), a positive charge is generated on electrode A to maintain the potential difference, thus generating a pulsed current from electrode A to electrode B in the external circuit (Figure 2A, state ii). The distance between the blades reaches the maximum under the dual effect of the wind field and feather structure (Figure 2A, state iii). As the blades rotate back to the windward position, the two triboelectric materials come into proximity with each other, resulting in the opposite flow of electrons through the external loads (Figure 2A, state iv). Electrode A re-establishes contact with the PTFE membrane, and the FI-TENG returns to the initial contact state (Figure 2A, state i).

The FI-TENG generates a continuous alternating current (AC) output through an internal circuit connection, as shown in Figure 2B. Three sets of blades are used so that the device can continuously harvest the wind (120° apart for each blade) while offering a good compromise between capturing wind energy and maintaining structural integrity. To interpret the current direction and potential distribution shown in Figure 2A, a finite element simulation of the electrostatic field was performed using COMSOL Multiphysics software. Figure 2C depicts the potential
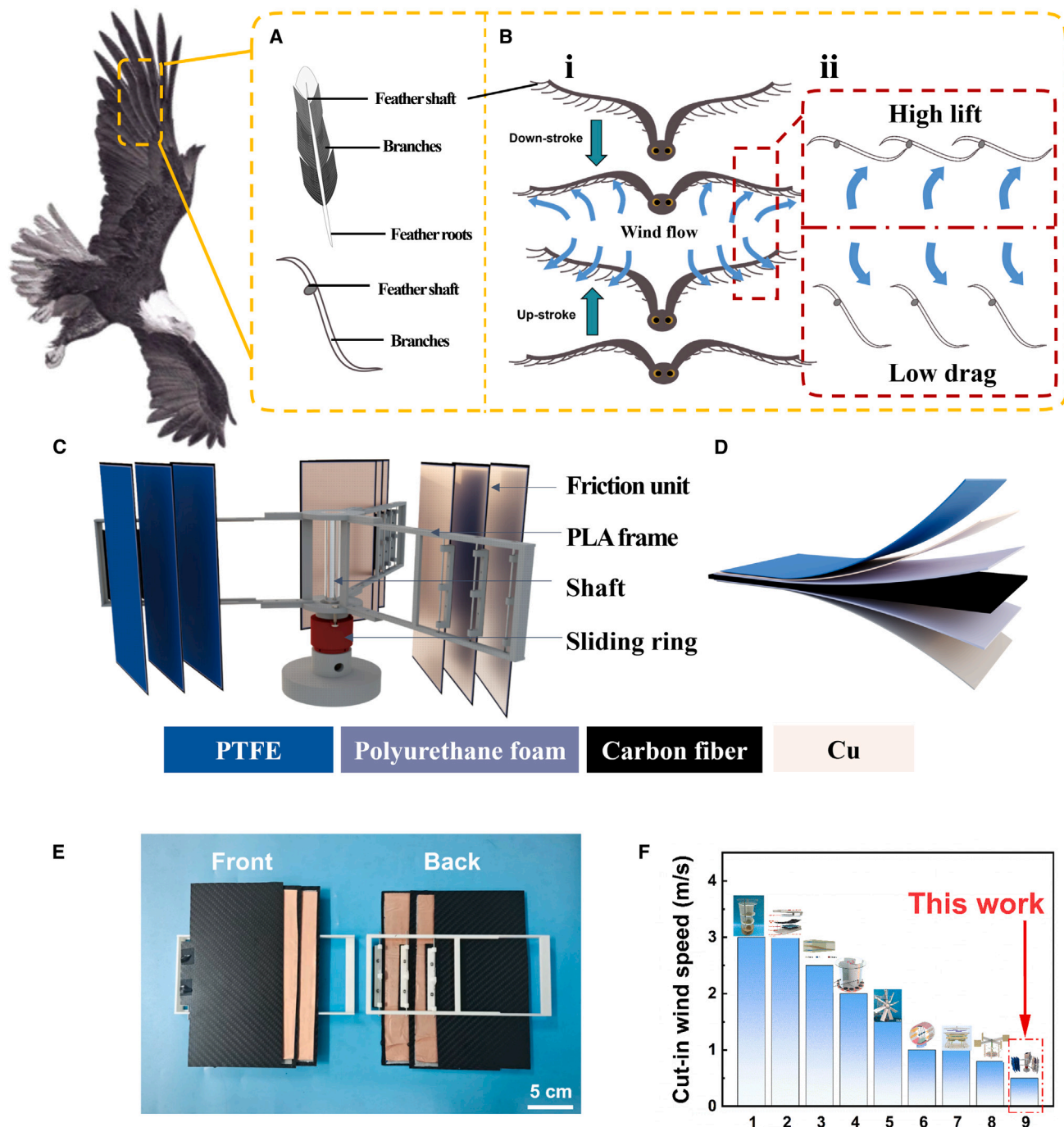
Figure 1. Biomimicry origin and structural design of the feather-inspired TENG

(A) Schematic diagram of bird feather structure.

(B) Schematic representation of the distribution of feathers in a bird in flight: (i) bird feather macro-motion demonstration and (ii) demonstration of high-lift, low-drag bird feather principle.

(C and D) Schematic structure of FI-TENG (C). (D) Detail of FI-TENG blade layer.

(E) FI-TENG leaf frame part of the physical picture.

(F) Comparison of cut-in wind speed between FI-TENG and other related equipment.

Device
Article

Device
Article

CellPress
OPEN ACCESS
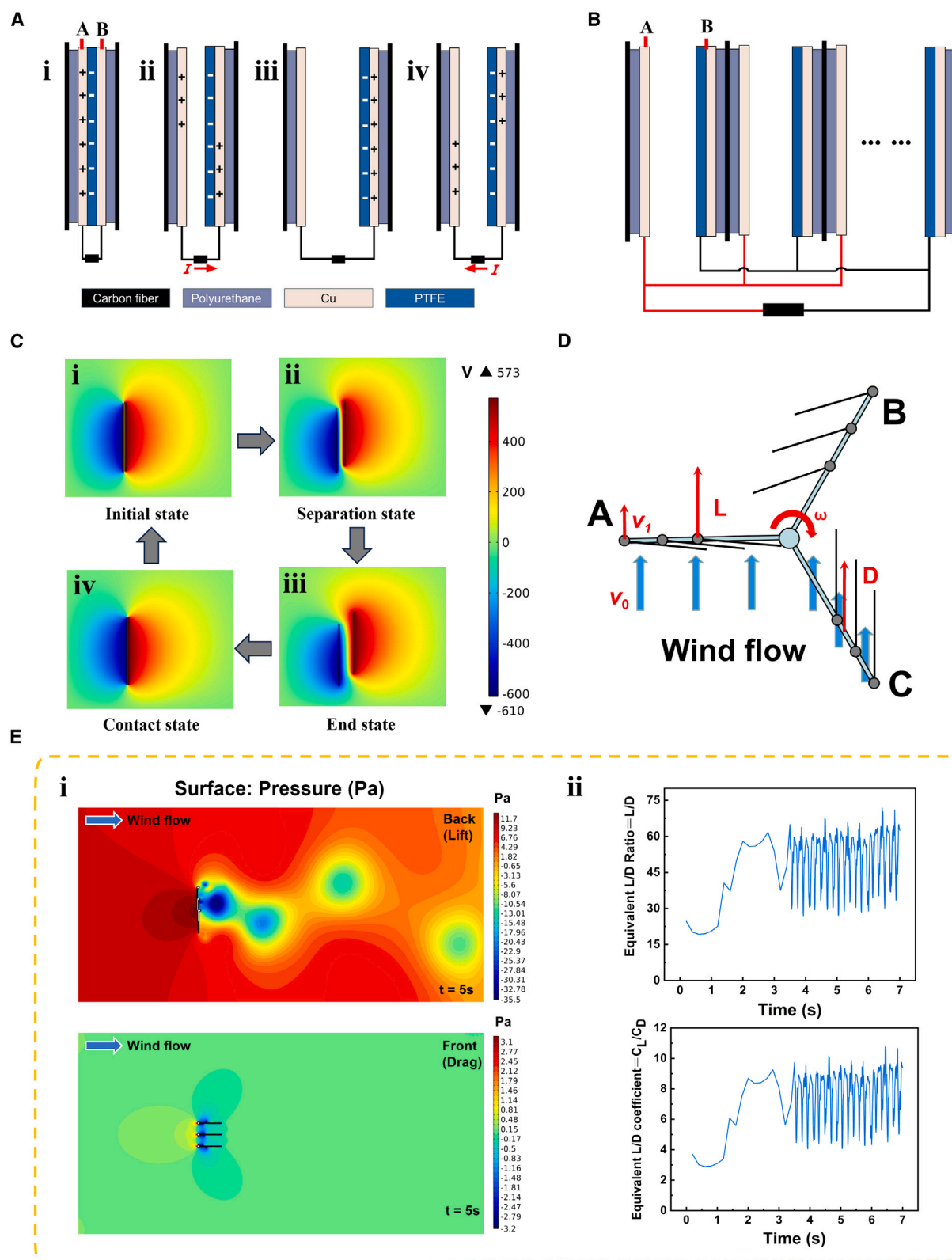
distribution and charge transfer direction between the Cu film and PTFE triboelectric materials.

To explain the overall motion mechanism of FI-TENG, we placed FI-TENG in a uniform wind field, as shown in Figure 2D. When the device is positioned in the continuous flow of the breeze, the blade in group A is on the windward side. Because of the blade shaft, the blades in blade group A are confined to one another and overlap as a single unit to provide rotational power to the FI-TENG. In this process, the blades touch one another, similar to the downward flapping process of a bird. When the back of blade group A is rotated to the windward side of the flow field, the same separation phenomenon as for blade group C will occur. Blade group C separates from one another and wind can pass through the blade gaps, similar to the upstroke phase of birds. These two processes alternate so that the FI-TENG rotates in a clockwise direction and completes the contact-separation cycle of the TENG.

Performance evaluation of the FI-TENG

To quantitatively and qualitatively evaluate the performance of FI-TENG from an aerodynamic point of view, we used COMSOL Multiphysics software to simulate the pressure and flow velocity distributions when the blade is in the laminar flow field, where the inlet flow velocity is 2.5 m/s. As can be seen from Figures 2D and 2E, the trajectory of the FI-TENG is not a standard vertical contact pattern, and there is a distance between the blades so that overlapping staggering can occur during operation. The setting of this distance has a direct effect on the collection efficiency of the FI-TENG. The analysis results show that the pressure at the back of the blade is much greater than that at the front, and it can use the force difference under the windward side to make a circular motion. Therefore, we quantitatively analyze the wing condition and the FI-TENG using an equivalent aerodynamic model, where we define the lift state as the FI-TENG windward backside case and the drag force as the FI-TENG windward frontal case.

Since the bird has a structural complexity, we simplify the analysis of the wing part by assuming that the bird is in a hovering state, and based on the kinetic equations[36] previously proposed by Usherwood and Ellington, we express the lift (L) as

$$L = \frac{1}{2}\rho C_L A_L (v_1 - v)^2 \qquad \text{(Equation 1)}$$

and set the drag force (D) to

$$D = \frac{1}{2}\rho C_D A_D (v_1 + v)^2, \qquad \text{(Equation 2)}$$

where ρ is the air density, C_L and C_D are the lift coefficient and drag coefficient, respectively (which are determined according

to the angle of attack of the bird during its movement), A_L and A_D are equivalent lift effective windward area and equivalent drag effective windward area, respectively, v_1 is the air velocity, and v is the blade linear velocity. For the bird model, the L/D changes as the angle of attack changes during motion, but because of the bird's own gravity, its L/D is usually maintained between 8 and 10 to complete the flight.[28,29,37–39] Here, we consider the case of the windward side of the FI-TENG at the stationary moment, when the FI-TENG does not rotate, $v = 0$. Its equivalent model satisfies the following conditions, and L/D can be obtained by dividing Equation 1 by Equation 2:

$$\frac{L}{D} = \frac{C_L}{C_D} * \frac{A_L}{A_D}, \qquad \text{(Equation 3)}$$

where L and D are simulated results and A_L and A_D are experimental data. As for the simulation, L/D can be directly obtained, and the value is around 45. In the same flow field, the effective area of the equivalent lifting surface is always greater than the effective area of the drag surface. From the comparison of Figures 2E and S1, it can be seen that $C_L \gg C_D$ and $\frac{C_L}{C_D}$ stays in the range of 4–9, which is close to the three-bucket Savonius wind turbine (same blade number as ours) designed by Gupta and Biswas[40] at much lower starting wind speeds.

In addition, we derive an L/D model for FI-TENG from the perspective of power maximization:

$$P = (L - D)v = \frac{1}{2}\rho \left[C_L A_L (v_1 - v)^2 - C_D A_D (v_1 + v)^2 \right]v, \qquad \text{(Equation 4)}$$

where P is the power, $C_L \gg C_D$ and $A_L \gg A_D$ are shown in Figure S1, and the difference between FI-TENG lift and drag is maximized when one side of the blade is parallel to the inlet. The specific flow velocity distribution is shown in Figure S2. The lift and drag sides of the FI-TENG maintain a large flow velocity difference, resulting in $L \gg D$. In the flow field, the FI-TENG always maintains the state of $v_1 \gg v$. FI-TENG can be used to maximize the power of the FI-TENG by using the parallel inlet wind state. Therefore, a comprehensive analysis confirms that during any given cyclic motion, there is always a moment when the blades of the FI-TENG are parallel to the direction of the incoming wind, which is achieved by the feather structure. The theoretical maximum output power of the FI-TENG can be obtained by substituting simulated C_L (around 5) and measured A_L (320 cm²).

Parameter optimization of the FI-TENG structure

To evaluate the possibility of stable operation of FI-TENG in a real-world environment, we developed a standard test procedure to optimize the output performance of FI-TENG by adjusting

Figure 2. Schematic diagram of FI-TENG's operating principle and COMSOL Multiphysics simulation validation
(A) Schematic of current and charge distribution in a short-circuit state.
(B) Schematic diagram of the working circuit connection of the blade set.
(C) Schematic of the electrical potential distribution in the open circuit state simulated by COMSOL Multiphysics.
(D) Schematic diagram of the overall coordination of FI-TENG's work.
(E) COMSOL Multiphysics simulation of the pressure distribution on the front and back of the FI-TENG as well as lift and drag analyses.
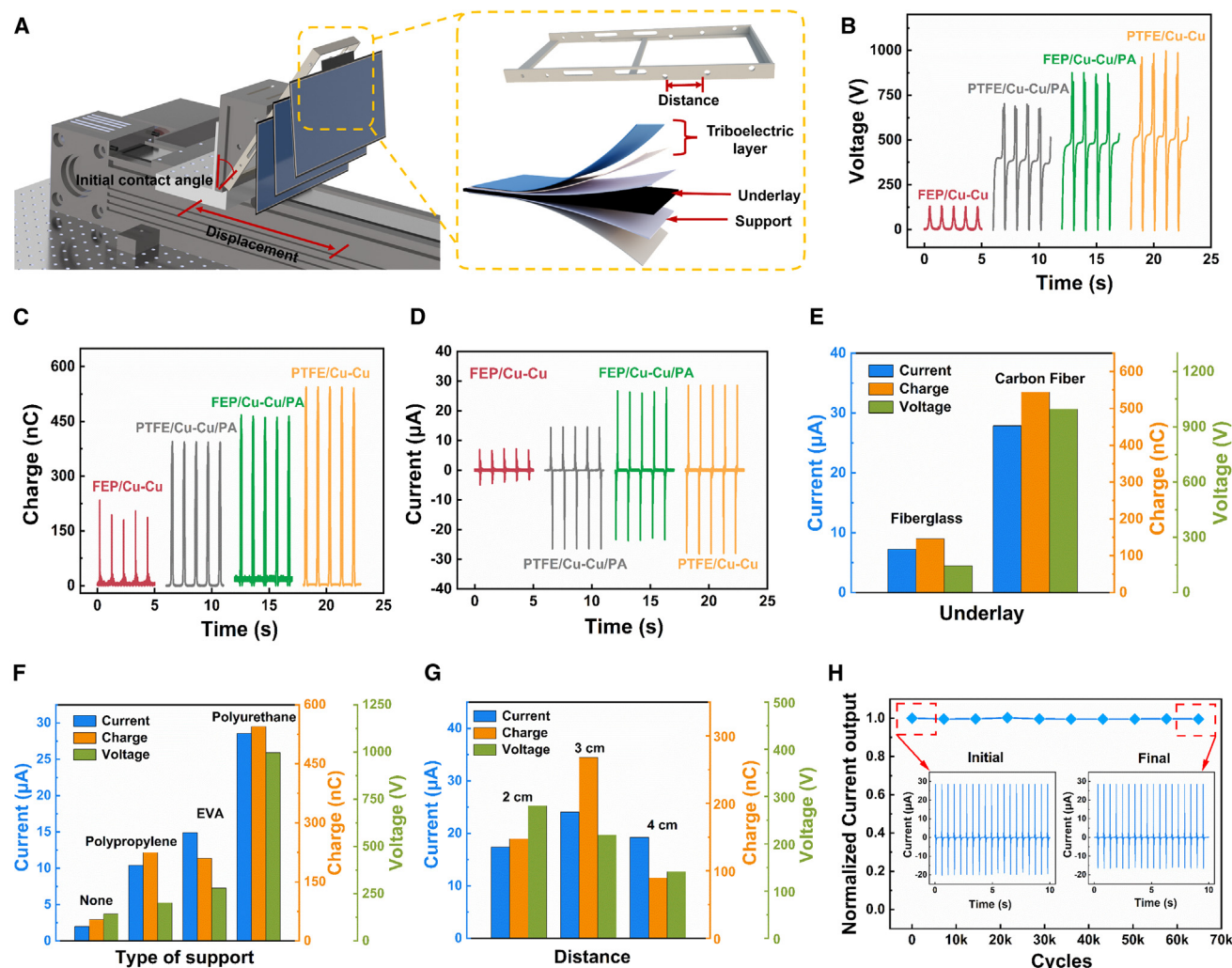
Figure 3. FI-TENG performance optimization

(A) Schematic diagram of the FI-TENG performance-optimized dynamic displacement test system. The inset shows a schematic of the four parameters that can be modified.

(B–D) Performance output with different triboelectric materials. (B) V_{oc}, (C) output charge, and (D) I_{sc}.

(E) Blade output performance with different underlay.

(F) Blade output performance with different support layers.

(G) Output performance for different blade distances.

(H) Durability test chart of the FI-TENG blade.

the triboelectric material, support layer structure, underlay material, and blade distance, as shown in Figure 3A. A detailed discussion of these parameters can be found in the following paragraphs.

The process of simplifying the operation of the linear motor involves adjusting the motor operating displacement (labeled in Figure 3A), controlling the test frequency, and setting the initial contact angle between the tool holder and the linear motor. To ensure comprehensive analysis, studying the output performance of only one type of movement is not sufficient. Therefore, we conducted tests to examine the displacement conditions that have the greatest impact on the output results of PTFE/Cu and Cu. As can be seen in Figure S3, the output of the triboelectric

layer is linearly correlated with the displacement of the linear motor within the 2- to 5-cm range. When the test displacement of the linear motor is greater than 5 cm, no contact occurs between the blades. To maintain the uniformity of the material test conditions, we finally chose 5 cm as the test standard.

As the triboelectric blade is a composite material and generates electrical signals directly, we focus on three polymer-organic materials, PTFE, fluorinated ethylene propylene (FEP), and polyamide (PA), combined as FEP/Cu-Cu, PTFE/Cu-Cu/PA, FEP/Cu-Cu/PA, and PTFE/Cu-Cu. The open-circuit voltage (V_{oc}), transferred charge (Q_{sc}) and short circuit current (I_{sc}) were tested on a linear motor with a frequency of 2 Hz and a stroke of 5 cm. From Figures 3B–3D, it can be concluded that

Device
Article

CellPress
OPEN ACCESS

the use of PTFE/Cu and Cu as the triboelectric layer has a better performance, with Q_{sc}s, V_{oc}s, and I_{sc}s up to 1,000 V, 550 nC, and 25 μA.[41]

The underlay serves as the structural foundation for the entire blade and plays a critical role in providing support. To meet the demands of lightweight design and high strength, we have evaluated two types of high-strength underlay materials: carbon fiber and glass fiber. These materials offer the necessary attributes to meet our requirements. Carbon fiber is known for its high strength and high modulus characteristics. Additionally, it possesses inherent conductive properties. Although the conductivity of carbon fiber decreases after undergoing epoxy resin impregnation treatment, it still retains its ability to attract and accumulate charges within the triboelectric layer on the surface of the blade, Thus, carbon fibers may have the ability to enhance the charge accumulation in the triboelectric layer.[42] Similarly, glass fiber is a high-strength material that offers superior insulation and mechanical strength compared to carbon fiber, but the final test results showed that the use of carbon fiber as a substrate output performance is much better than glass fiber, which may confirm our speculation that the internal conductive properties of carbon fiber materials can improve the output performance of FI-TENG as shown in Figures 3E and S4.

The support layer is vital for the performance of the FI-TENG, as it acts as an interface between the triboelectric layer and the bottom layer. It helps mitigate issues such as blade collisions and insufficient contact, optimizing the overall efficiency of the system. We have selected three insulating soft polymer materials of equal size for evaluation: polypropylene film (1.5 g), ethylene-vinyl acetate foam (4 g), and polyurethane sponge (1 g). As can be seen from Figures 3F and S5, under the same test conditions, all the performances of the blades with the added support layer are significantly higher than those without. This observation provides evidence that the support layer improves the performance of FI-TENG blades. Polyurethane foam is lighter in weight and exhibits double the V_{oc}, I_{sc}, and Q_{sc} compared to the other materials. These superior performance characteristics make it an ideal choice for the support layer in the FI-TENG system.

Furthermore, based on the TENG-induced charge generation equation, modifying the spacing between the blades alters the overlap area between them. As a result, this adjustment influences the size of the polarization field area.[9] As depicted in Figure 3G, it is evident that maintaining a blade spacing of 2 cm results in the largest overlapping area. However, it is worth noting that this configuration also leads to the highest electrostatic force produced by the triboelectric layer. This in turn affects the opening and closing cycles of the blades. Blades with a spacing of 3 cm demonstrate the advantage of high efficiency combined with low electrostatic force, as shown in Figure S6. Furthermore, we also present the durability test results of the FI-TENG blades in Figure 3H. After 10 h of continuous testing with 72,000 contact cycles, the performance of the FI-TENG blades remained at a high performance level. Similarly, we tested the effect of humidity on the power-generation unit accordingly, as shown in Figure S7, where the current output of the power-generation unit remains essentially unchanged as the relative humidity changes. Figure S8 provides visual representation of this exploration. This ensures that the results of the FI-TENG's linear motor tests can be accurately analyzed, providing the best guidance strategy for subsequent testing in real wind environments.

FI-TENG performance under fan conditions

To verify the viability of the FI-TENG under low wind speeds, we conducted testing using a wind turbine as a source of wind. Figures 4A and 4B illustrate the output performance, specifically the I_{sc} and the Q_{sc}, of a single set of FI-TENG blades at various wind speeds. The wind turbine used in our testing allows for the adjustment of wind speeds within the range of 0–5 m s^{-1}. However, we focused on assessing the performance of the FI-TENG at low wind speeds ranging from 0–2.5 m s^{-1}. By examining Figure 4, it is evident that both current and voltage exhibit an upward trend as the wind speed increases within the specified range. Notably, when the wind speed reaches 0.5–1 m s^{-1}, the blades meet the minimum startup requirements, with the I_{sc} reaching 5 μA and the Q_{sc} reaching 25 nC. As the wind speed surpasses 1.5–2.5 m s^{-1}, the I_{sc} reaches 15 μA, and the Q_{sc} reaches 150 nC. Under the same wind speed conditions, the saturated state of each output is 1.5–2 times more than other similar types of wind energy collection equipment.[43]

To ensure the accuracy of our analysis, we performed routine performance tests on three groups of FI-TENG blades under identical conditions designed to eliminate differences between the groups that might affect the assessment. Under the same wind speed condition of 1.5 m s^{-1}, we tested the performance of FI-TENG when each blade group A, B, C works alone, as shown in Figure 4C; the error range of the V_{oc} of the three blade groups is kept at ±10%. Subsequently, we conducted experiments to explore the impact of the simultaneous operation of different groups of blades on the overall performance of FI-TENG. The operation of groups A, AB, and ABC were tested separately to assess their respective contributions to the overall performance of the FI-TENG at 2.5 m s^{-1}, as shown in Figure 4D. When both blades are in operation, the FI-TENG system exhibits a peak current of 15 μA, which is three times higher than comparable studies with the same number of generating units. Moreover, when all 10 units are running simultaneously, the overall output current of the FI-TENG with its three blades reaches an even higher value of 27.4 μA.[41]

To rectify the outputs from different groups, we connected three sets of blades in parallel to the rectifier to test the rectified output power. As can be seen from Figures 4E and 4F, the synergistic effect of the blade set significantly improves the overall performance of the FI-TENG as the wind speed increases, and the I_{sc} and V_{oc} of the FI-TENG reach their maximum values of 27.4 μA and 470 V, respectively, at 2.5 m s^{-1}. Tests in fan conditions over a long period of time are detailed in Figure S9. In addition, we evaluate the overall output performance of the FI-TENG system during the application phase and demonstrate its ability to charge capacitors, as shown in Figures 4G and 4H. Figure 4G illustrates the voltage profiles of the FI-TENG while charging capacitors with various capacitances at a wind speed of 2.5 m s^{-1} in 60 s. The charging efficiency of FI-TENG is higher under the same conditions as compared to other similar types of work.[43] Figure 4H shows the charging voltage curves for a 100-μF capacitor at different wind speeds, where we set the wind speed gradient to 0.5–2.5 m s^{-1} and the charging rate increases with
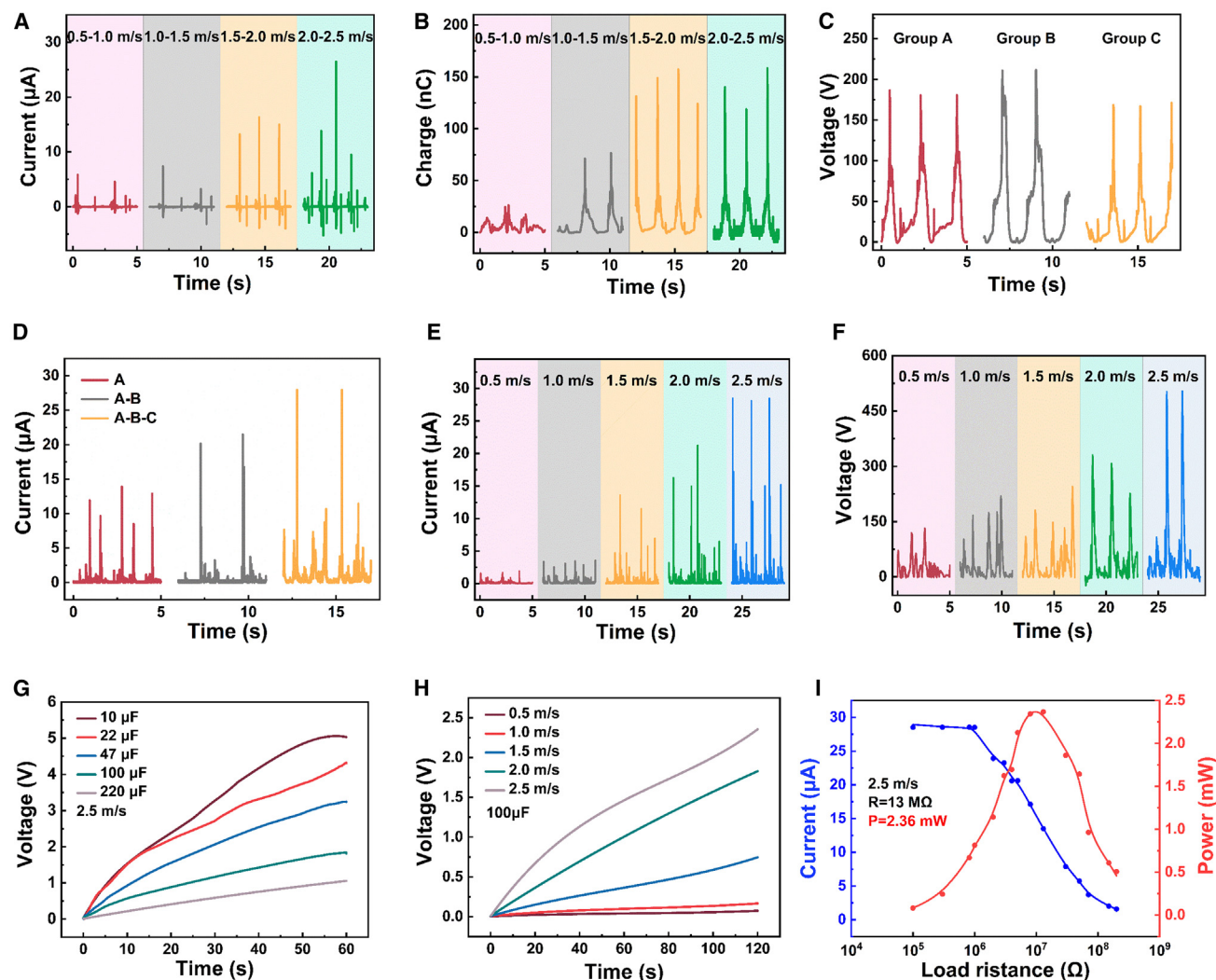
Figure 4. Characterization of the output performance of FI-TENG under fan conditions for single set of blades operation and overall operation

(A and B) Single set of blades at different wind speeds. (A) I_{sc}, (B) transferred charge.

(C) V_{oc} test for different groups of blades.

(D) I_{sc} test performance when accessing different sets of blades accordingly.

(E and F) Overall output performance of FI-TENG at different wind speeds. (E) I_{sc} and (F) V_{oc}.

(G) Charging performance curves of capacitors with different capacities at 2.5 m s^{-1}.

(H) Charging characteristics of 100-μF capacitors at different wind speeds.

(I) Output power and instantaneous peak current-resistance relationship of FI-TENG at 2.5 m s^{-1}.

the wind speed. To evaluate the matched impedance and the peak power of the FI-TENG device, its output performances are tested with a series of different load resistances at a wind speed of 2.5 m s^{-1}. As illustrated in Figure 4I, the output current has a horizontal trend when the resistance is small. The output current gradually decreases with increased external load resistance, and the output power rise and then falls. A peak power of 2.36 mW is obtained under a load resistance of 13 MΩ.

Application of the FI-TENG device

The modular structural design as shown in Figure 5A can achieve the effect of high-efficiency collection of breeze energy. FI-TENG

as a contact-separation mode has lower wear than a traditional rotary TENG in freestanding mode for low-frequency wind energy harvesting, achieving high power output while minimizing the breakdown voltage risk and reducing the application failure rate.[44] Moreover, the uneven force during the operation of the rotating TENG can cause extra losses in the triboelectric layer,[45] as opposed to FI-TENG, which reduces this loss by incorporating a support layer. This enables the FI-TENG to harness wind energy in natural environments with low-frequency and low-wind speeds, using its feathered structural features.

To enable the charging functionality of the FI-TENG, an energy management (EM) circuit is employed to enhance the output
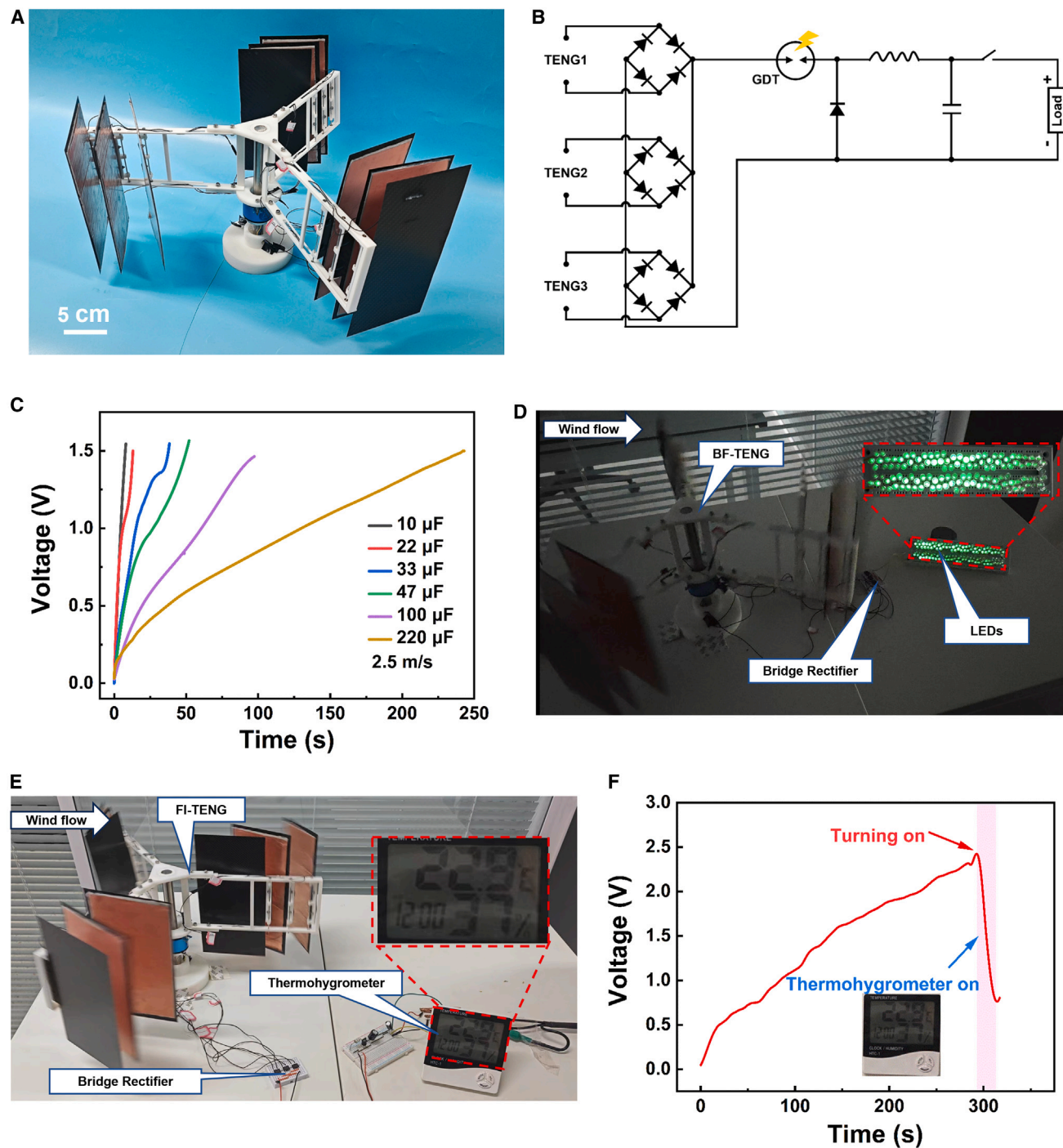
Figure 5. Application demonstration of the FI-TENG device

(A) Physical drawing of the assembly of the FI-TENG; the experimental procedures discuss the detailed manufacturing process of each part.

(B) Schematic diagram of EM circuit.

(C) Charging characteristic curves of different capacitors after connecting the circuit.

(D) FI-TENG lights up 120 LEDs.

(E) Photographs and demonstrations of FI-TENG powering a thermo-hygrometer.

(F) The FI-TENG powers a commercial thermo-hygrometer for 5 min to keep it working for 10 s.

performance of the FI-TENG. A detailed description of the EM circuit can be found in Note S1. Figure 5B illustrates the specific details of the management circuitry. The EM circuit utilizes a gas discharge tube as a switch to facilitate the accumulation and release of the harvested energy. This configuration enhances the capability of the FI-TENG to instantaneously and rapidly charge various types of capacitors. As depicted in Figures 5C and S10, the incorporation of the management circuit leads to a 2.5 times improvement in charging speed compared to the condition without the circuit. We note, in particular, that a 100-µF capacitor can be charged to 1.5 V within a duration of 250 s.

After completing the basic circuit optimization, we conducted an application demonstration under a wind speed of 2.5 m s^{-1}. As depicted in Figure 5D and demonstrated in Video S1, we showcased the capability of the FI-TENG to power 120 light-emitting diodes (LEDs) with stable operation, which shows that the FI-TENG is capable of providing stable self-powered conditions for low-power alarm indicators. Figures 5E and 5F illustrate the test system utilized for the FI-TENG. The entire system is charged by the fan drive for approximately 300 s, resulting in the voltage of the 220-µF capacitor reaching 2.4 V. Importantly, this charged capacitor serves as the power supply for commercial temperature and humidity sensors, enabling normal operation of the thermo-hygrometer. The demonstration of the thermo-hygrometer's normal functioning is presented in Video S2. Due to the wind collection performance and low initial wind speed requirement of the FI-TENG, the device can be installed on both sides of walkways to serve as a walkway indicator and a sensor to gather ambient temperature and humidity information.

Conclusion and outlook

We have designed a feather-inspired TENG for wind energy harvesting by mimicking the structures and dynamics of bird feathers during wing flapping. The integration of wind power harvesting into the biomimetic feather blade structure reduces weight and friction and improves the L/D of the FI-TENG, which reduces the start-up wind speed and increases the energy conversion efficiency. The FI-TENG can power a commercially available thermo-hygrometer and 120 LEDs, which can be used as indicators for nature trails and can also monitor the temperature and humidity of the trail environment in real time to provide rational guidance for urban planning and design. FI-TENG has the potential to become a distributed energy harvesting solution, complementing large wind turbines for low wind speed wind energy harvesting.

Looking forward, several areas of development are crucial for advancing FI-TENG technology. The development and integration of low-consumption circuits and sensors will be essential to maximize the efficiency and practicality of the device in various applications. Additionally, scalable designs tailored for different wind conditions and power requirements are needed to expand the utility of FI-TENG, whether in urban environments, remote landscapes, or industrial settings. Finally, exploring industrial manufacturing techniques or alternative designs will be vital to enable mass production and widespread adoption, ensuring that FI-TENG can meet the demands of diverse energy harvesting needs in the future.

EXPERIMENTAL PROCEDURES

Manufacture of the FI-TENG

The FI-TENG power-generation unit consists of nine blades, three groups, three per group. The three blades are attached to the blade frame by connectors, and the groups are separated by 120°. The carbon fiber plate (0.2 mm), which is the base, has a layer of polyurethane sponge (1 mm) on both the upper and lower surfaces, a composite layer of PTFE film (30 µm) and Cu film (25 µm) on the upper surface, and a layer of Cu film (25 µm) on the lower surface. The dimensions of the specifics are as follows: carbon fiber (20 cm × 10 cm × 0.2 mm), polyurethane sponge (18.5 cm × 8.5 cm × 1 mm), PTFE (19 cm × 9 cm × 30 µm), and Cu (18.5 × 18.5 × 25 µm). Raw material suppliers include PTFE (Nippon Zeon Corporation, ASF-110FR), Cu (Suzhou Qian Ding Li Electronic Technology, 0.03MM), FEP (Daikin Industries, NEOFLON FEP NP), carbon fiber (Toray), and glass fiber (Shenzhen Yifeng Insulation Material, FR-4).

The overall height of FI-TENG is 26 cm and the width is 40 cm. The frame of the FI-TENG is 3D-printed (Tiertime UP300) using PLA material and consists of the connectors (irregular cover plate with a radius of 6.5 cm), the blade frame (length 20 cm, width 9 cm), and the base (diameter 10 cm). The 3D-printed parts are held together by a stainless-steel optical shaft (15 mm diameter, 200 mm long) and ceramic bearings. The energy harvesting area uses an electrically conductive sliding ring (H1542-0605TC, Senring) to channel the energy harvested from the blade area into the power management circuit, the sliding ring (inner diameter 1.5 cm, outer diameter 4.2 cm). Finally, it is fixed to the platform by the base.

Electrical measurements

All the equipment was fixed on an optical stage (YH-LPB, Yihang) for testing using linear motors (R-LP4/DA-ARM1651, Naneng) for linear motion; an electrostatic meter (6514, Keighley) to measure the I_{sc}s, Q_{sc}s, and V_{oc}s; and a fan (SE-A200, Sensdar) controlled by an AC speed regulator (ZADY6000X, CHNK), with a digital anemometer (9565-NB, TSI) for testing the wind speed.

COMSOL simulation

COMSOL Multiphysics was used to simulate the electric potential distribution of TENG. The steady-state potential distribution characteristics of TENG are investigated in a two-dimensional (2D) plane using an electrostatic field. The software also is used to simulate the surface flow velocity and the drag and lift forces on the TENG when it is in a laminar flow field. The fluid transient characteristics of TENG when it is on the windward and leeward sides are investigated on a 2D plane using the unidirectional flow laminar module. Further details can be found in Note S2.

RESOURCE AVAILABILITY

Lead contact

Requests for further information, resources, and reagents should be directed to and will be fulfilled by the lead contact, L.N.Y. Cao (caonanying@binn.cas.cn).

Materials availability

The materials generated in this study are available from the lead contact upon reasonable request.

Data and code availability

The data used to support the findings of this study are available from the lead contact upon reasonable request.

Device
Article

AUTHOR CONTRIBUTIONS

Z.D., E.S., and L.N.Y.C. contributed to the research conceptualization and methodology, conducted the experimental validation, and wrote and revised the original manuscript. Z.D. and L.N.Y.C. contributed to the theoretical calculations. Z.D. and H.Y. contributed to the fabrication of the TENG. Z.D. and Z.H. contributed to the software programming. Z.L.W. and L.N.Y.C. supervised and performed project administration. All authors discussed the results and commented on the manuscript.

DECLARATION OF INTERESTS

The authors declare no competing interests.

SUPPLEMENTAL INFORMATION

REFERENCES

1. Cao, L.N.Y., Xu, Z., and Wang, Z.L. (2022). Application of Triboelectric Nanogenerator in Fluid Dynamics Sensing: Past and Future. Nanomaterials 12, 3261. https://doi.org/10.3390/nano12193261.

2. Cao, Y., Su, E., Sun, Y., Wang, Z.L., and Cao, L.N.Y. (2024). A Rolling-Bead Triboelectric Nanogenerator for Harvesting Omnidirectional Wind-Induced Energy toward Shelter Forests Monitoring. Small 20, e2307119. https://doi.org/10.1002/smll.202307119.

3. Hasan, M.A.M., Zhu, W., Bowen, C.R., Wang, Z.L., and Yang, Y. (2024). Triboelectric nanogenerators for wind energy harvesting. Nat. Rev. Electr. Eng. 1, 453–465. https://doi.org/10.1038/s44287-024-00061-6.

4. Wang, Y., Wang, J., Li, H., Gao, Q., Zhu, M., Su, T., Wang, Y., Cheng, X., and Cheng, T. (2024). Steady Output Triboelectric-Electromagnetic Hybrid Generator with Variable Drag Turbine Blades for Natural Wind Energy Harvesting. ACS Appl. Mater. Interfaces 16, 39287–39294. https://doi.org/10.1021/acsami.4c05790.

5. Zhu, M., Zhu, J., Zhu, J., Zhao, Z., Li, H., Cheng, X., Wang, Z.L., and Cheng, T. (2024). Bladeless Wind Turbine Triboelectric Nanogenerator for Effectively Harvesting Random Gust Energy. Adv. Energy Mater. https://doi.org/10.1002/aenm.202401543.

6. Wang, Z.L., Jiang, T., and Xu, L. (2017). Toward the blue energy dream by triboelectric nanogenerator networks. Nano Energy 39, 9–23. https://doi.org/10.1016/j.nanoen.2017.06.035.

7. Xu, S., Zhang, J., Su, E., Li, C., Tang, W., Liu, G., Cao, L.N., and Wang, Z.L. (2024). Dynamic behavior and energy flow of floating triboelectric nanogenerators. Appl. Energy 367, 123468. https://doi.org/10.1016/j.apenergy.2024.123468.

8. Xi, Y., Hua, J., and Shi, Y. (2020). Noncontact triboelectric nanogenerator for human motion monitoring and energy harvesting. Nano Energy 69, 104390. https://doi.org/10.1016/j.nanoen.2019.104390.

9. Niu, S., and Wang, Z.L. (2015). Theoretical systems of triboelectric nanogenerators. Nano Energy 14, 161–192. https://doi.org/10.1016/j.nanoen.2014.11.034.

10. Xu, Z., Cao, L.N., and Wang, Z.L. (2024). Triboelectric Nanogenerators for Scientific Instruments and Devices. Adv. Devices Instrum. 5. https://doi.org/10.34133/adi.0026.

11. Xu, Z., Cao, L.N.Y., Li, C., Luo, Y., Su, E., Wang, W., Tang, W., Yao, Z., and Wang, Z.L. (2023). Digital mapping of surface turbulence status and aerodynamic stall on wings of a flying aircraft. Nat. Commun. 14, 2792. https://doi.org/10.1038/s41467-023-38486-6.

12. Liu, C., Li, J., Che, L., Chen, S., Wang, Z., and Zhou, X. (2017). Toward large-scale fabrication of triboelectric nanogenerator (TENG) with silk-fibroin patches film via spray-coating process. Nano Energy 41, 359–366. https://doi.org/10.1016/j.nanoen.2017.09.038.

13. Chen, S.W., Cao, X., Wang, N., Ma, L., Zhu, H.R., Willander, M., Jie, Y., and Wang, Z.L. (2017). An Ultrathin Flexible Single-Electrode Triboelectric-Nanogenerator for Mechanical Energy Harvesting and Instantaneous Force Sensing. Adv. Energy Mater. 7, 1601255. https://doi.org/10.1002/aenm.201601255.

14. Yao, L., Zhou, Z., Zhang, Z., Du, X., Zhang, Q.-L., and Yang, H. (2022). Dyeing-Inspired Sustainable and Low-Cost Modified Cellulose-Based TENG for Energy Harvesting and Sensing. ACS Sustainable Chem. Eng. 10, 3909–3919. https://doi.org/10.1021/acssuschemeng.1c08095.

15. Zhang, M., Han, C., Cao, W.-Q., Cao, M.-S., Yang, H.-J., and Yuan, J. (2020). A Nano-Micro Engineering Nanofiber for Electromagnetic Absorber, Green Shielding and Sensor. Nano-Micro Lett. 13, 27. https://doi.org/10.1007/s40820-020-00552-9.

16. Wang, D., Zhang, D., Yang, Y., Mi, Q., Zhang, J., and Yu, L. (2021). Multifunctional Latex/Polytetrafluoroethylene-Based Triboelectric Nanogenerator for Self-Powered Organ-like MXene/Metal–Organic Framework-Derived CuO Nanohybrid Ammonia Sensor. ACS Nano 15, 2911–2919. https://doi.org/10.1021/acsnano.0c09015.

17. Zhang, H., Zhang, D., Mao, R., Zhou, L., Yang, C., Wu, Y., Liu, Y., and Ji, Y. (2024). MoS2-based charge trapping layer enabled triboelectric nanogenerator with assistance of CNN-GRU model for intelligent perception. Nano Energy 127, 109753. https://doi.org/10.1016/j.nanoen.2024.109753.

18. Yu, J., Xian, S., Zhang, Z., Hou, X., He, J., Mu, J., Geng, W., Qiao, X., Zhang, L., and Chou, X. (2023). Synergistic piezoelectricity enhanced BaTiO3/polyacrylonitrile elastomer-based highly sensitive pressure sensor for intelligent sensing and posture recognition applications. Nano Res. 16, 5490–5502. https://doi.org/10.1007/s12274-022-5084-x.

19. Zhang, Z., Jie, Y., Zhu, J., Zhu, Z., Chen, H., Lu, Q., Zeng, Y., Cao, X., Wang, N., and Wang, Z. (2021). Paper triboelectric nanogenerator designed for continuous reuse and quick construction. Nano Res. 15, 1109–1114. https://doi.org/10.1007/s12274-021-3612-8.

20. Chen, H., Lu, Q., Cao, X., Wang, N., and Wang, Z.L. (2021). Natural polymers based triboelectric nanogenerator for harvesting biomechanical energy and monitoring human motion. Nano Res. 15, 2505–2511. https://doi.org/10.1007/s12274-021-3764-6.

21. Li, H., Zhang, Y., Gao, Z., Liang, L., Wang, X., Liu, X., Wu, Y., and Zheng, H. (2023). Modular design and fully packed triboelectric nanogenerator based on escapement mechanism for harvesting high entropy energy in harsh environments. Nano Energy 109, 108266. https://doi.org/10.1016/j.nanoen.2023.108266.

22. Yu, J., Xian, S., Mu, J., Wang, M., Wang, Y., Hou, X., Zhang, L., He, J., Mu, J., and Chou, X. (2023). Hybrid electromechanical properties of hetero-doped and homogeneously bonded dual-mode pressure sensor for indoor body area network node. Sci. China Inf. Sci. 67, 112401. https://doi.org/10.1007/s11432-023-3801-1.

23. Liu, D., Chen, B., An, J., Li, C., Liu, G., Shao, J., Tang, W., Zhang, C., and Wang, Z.L. (2020). Wind-driven self-powered wireless environmental sensors for Internet of Things at long distance. Nano Energy 73, 104819. https://doi.org/10.1016/j.nanoen.2020.104819.

24. Liu, Y., Zhu, M., Nan, D., Li, X., Wang, Y., Su, W., Wang, Z.L., and Cheng, T. (2022). Enhanced Durability and Robustness of Triboelectric Nanogenerators with Blade-Enclosed Structure for Breeze Energy Harvesting. Adv. Sustain. Syst. 7, 2200367. https://doi.org/10.1002/adsu.202200367.

25. Su, E., Li, H., Zhang, J., Xu, Z., Chen, B., Cao, L.N., and Wang, Z.L. (2023). Rationally Designed Anti-Glare Panel Arrays as Highway Wind Energy Harvester. Adv. Funct. Mater. 33, 2214934. https://doi.org/10.1002/adfm.202214934.

26. Zhu, M., Zhang, J., Wang, Z., Yu, X., Zhang, Y., Zhu, J., Wang, Z.L., and Cheng, T. (2022). Double-blade structured triboelectric–electromagnetic hybrid generator with aerodynamic enhancement for breeze energy harvesting. Appl. Energy 326, 119970. https://doi.org/10.1016/j.apenergy.2022.119970.

27. Cao, L.N., Su, E., Xu, Z., and Wang, Z.L. (2023). Fully enclosed microbeads structured TENG arrays for omnidirectional wind energy harvesting with a portable galloping oscillator. Mater. Today 71, 9–21. https://doi.org/10.1016/j.mattod.2023.11.001.

28. Howey, D.A., Bansal, A., and Holmes, A.S. (2011). Design and performance of a centimetre-scale shrouded wind turbine for energy harvesting. Smart Mater. Struct. 20, 085021. https://doi.org/10.1088/0964-1726/20/8/085021.

29. Mueller, T.J. (2001). Fixed and Flapping Wing Aerodynamics for Micro Air Vehicle Applications (American Institute of Aeronautics and Astronautics).

30. Lingham-Soliar, T. (2017). Microstructural tissue-engineering in the rachis and barbs of bird feathers. Sci. Rep. 7, 45162. https://doi.org/10.1038/srep45162.

31. Dial, K.P., Jackson, B.E., and Segre, P. (2008). A fundamental avian wing-stroke provides a new perspective on the evolution of flight. Nature 451, 985–989. https://doi.org/10.1038/nature06517.

32. Lu, P., Pang, H., Ren, J., Feng, Y., An, J., Liang, X., Jiang, T., and Wang, Z.L. (2021). Swing-Structured Triboelectric–Electromagnetic Hybridized Nanogenerator for Breeze Wind Energy Harvesting. Adv. Mater. Technol. 6, 2100496. https://doi.org/10.1002/admt.202100496.

33. Tcho, I.W., Kim, W.G., Kim, J.K., Kim, D.W., Yun, S.Y., Son, J.H., and Choi, Y.K. (2022). A flutter-driven triboelectric nanogenerator for harvesting energy of gentle breezes with a rear-fixed fluttering film. Nano Energy 98, 107197. https://doi.org/10.1016/j.nanoen.2022.107197.

34. Zhang, B., Gao, Q., Li, W., Zhu, M., Li, H., Cheng, T., and Wang, Z.L. (2023). Alternating Magnetic Field-Enhanced Triboelectric Nanogenerator for Low-Speed Flow Energy Harvesting. Adv. Funct. Mater. 33, 2304839. https://doi.org/10.1002/adfm.202304839.

35. Zhu, X., Cao, X., and Wang, Z.L. (2022). Windmill-Like Nanogenerator for Harvesting Low-Speed Wind Energy and Wind Speed Measuring. Adv. Mater. Technol. 7, 2200006. https://doi.org/10.1002/admt.202200006.

36. Crandell, K.E., and Tobalske, B.W. (2011). Aerodynamics of tip-reversal upstroke in a revolving pigeon wing. J. Exp. Biol. 214, 1867–1873. https://doi.org/10.1242/jeb.051342.

37. Muijres, F.T., Bowlin, M.S., Johansson, L.C., and Hedenström, A. (2012). Vortex wake, downwash distribution, aerodynamic performance and wingbeat kinematics in slow-flying pied flycatchers. J. R. Soc. Interface 9, 292–303. https://doi.org/10.1098/rsif.2011.0238.

38. Hedenström, A., Rosén, M., and Spedding, G.R. (2006). Vortex wakes generated by robins Erithacus rubecula during free flight in a wind tunnel. J. R. Soc. Interface 3, 263–276. https://doi.org/10.1098/rsif.2005.0091.

39. Chin, D.D., and Lentink, D. (2019). Birds repurpose the role of drag and lift to take off and land. Nat. Commun. 10, 5354. https://doi.org/10.1038/s41467-019-13347-3.

40. Gupta, R., and Biswas, A. (2011). CFD Analysis of Flow Physics and Aerodynamic Performance of a Combined Three-Bucket Savonius and Three-Bladed Darrieus Turbine. Int. J. Green Energy 8, 209–233. https://doi.org/10.1080/15435075.2010.548541.

41. Feng, L., Wang, Z.L., Cao, X., and Zhang, L. (2023). Accordion-inspired parallelly assembled triboelectric nanogenerator: For efficient biomechanical energy harvesting and music responding. Nano Today 49, 101760. https://doi.org/10.1016/j.nantod.2023.101760.

42. Fu, Y., Tian, Y., Li, M., Ma, J., Li, S., Zhu, W., Yan, K., and Ke, Y. (2022). Electrostatic manipulation for saturated charging and orientating of recycled short-chopped carbon fibers based on dielectric polarization. J. Clean. Prod. 380, 134912. https://doi.org/10.1016/j.jclepro.2022.134912.

43. Li, H., Wen, J., Ou, Z., Su, E., Xing, F., Yang, Y., Sun, Y., Wang, Z.L., and Chen, B. (2023). Leaf-Like TENGs for Harvesting Gentle Wind Energy at An Air Velocity as Low as 0.2 m s−1. Adv. Funct. Mater. 33, 2212207. https://doi.org/10.1002/adfm.202212207.

44. Ma, G., Wang, D., Wang, J., Li, J., Wang, Z., Li, B., Mu, Z., Niu, S., Zhang, J., Ba, K., et al. (2023). A durable triboelectric nanogenerator with a coaxial counter-rotating design for efficient harvesting of random mechanical energy. Nano Energy 105, 108006. https://doi.org/10.1016/j.nanoen.2022.108006.

45. Liu, D., Li, C., Chen, P., Zhao, X., Tang, W., and Wang, Z.L. (2022). Sustainable Long-Term and Wide-Area Environment Monitoring Network Based on Distributed Self-Powered Wireless Sensing Nodes. Adv. Energy Mater. 13, 2202691. https://doi.org/10.1002/aenm.202202691.